

Topological Feature Tracking for Submesoscale Eddies

Sam Voisin¹, Jay Hineman¹, James Bruce Polly², Gary Koplík¹, Ken Ball¹, Paul Bendich¹, Joseph D'Addezio³, Gregg A Jacobs⁴, and Tamay M. M. Ozgokmen⁵

¹Geometric Data Analytics

²Geometric Data Analytics, Inc.

³Naval Research Laboratory Ocean Dynamics & Prediction Branch

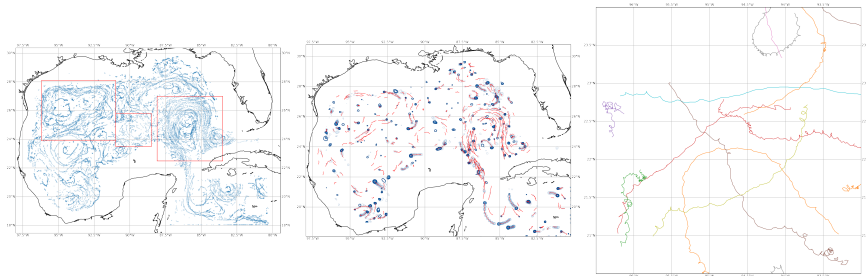
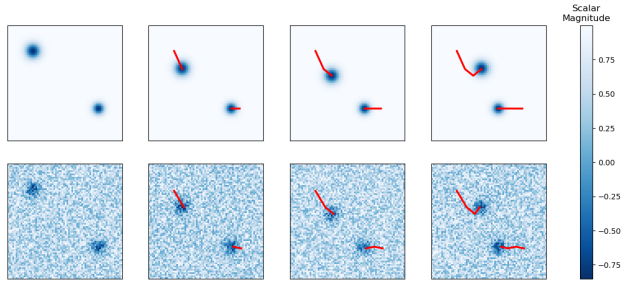
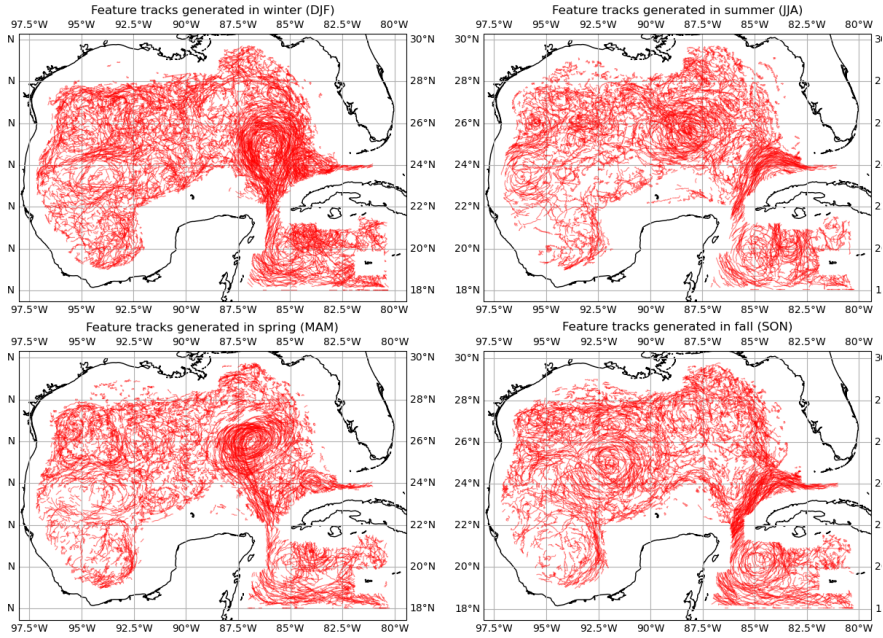
⁴Naval Research Laboratory

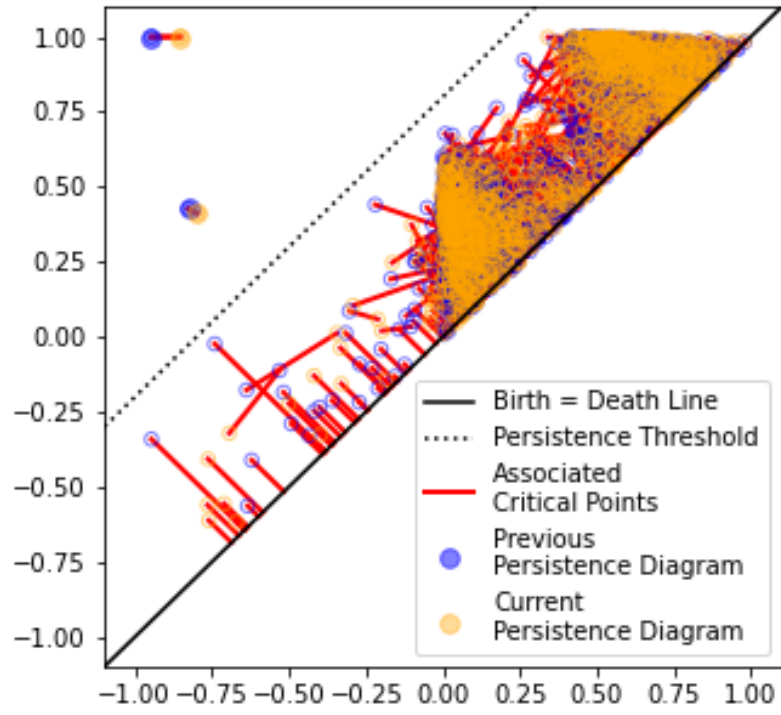
⁵University of Miami

November 23, 2022

Abstract

Current state-of-the-art procedures for studying modeled submesoscale oceanographic features have made a strong assumption of independence between features identified at different times. Therefore, all submesoscale eddies identified in a time series were studied in aggregate. Statistics from these methods are illuminating but oversample identified features and cannot determine the lifetime evolution of the transient submesoscale processes. To this end, the authors apply the Topological Feature Tracking (TFT) algorithm to the problem of identifying and tracking submesoscale eddies over time. TFT allows a user to identify submesoscale eddies as critical points on a set of time-ordered scalar fields and associate the points between consecutive timesteps. The procedure yields tracklets which represent spatio-temporal displacement of eddies. Thus the time-dependent behavior of submesoscale eddies can be studied. We analyze the submesoscale eddy dataset produced by TFT, which yields unique, time-varying statistics on this currently underexplored phenomenon.





Topological Feature Tracking for Submesoscale Eddies

Sam Voisin¹, Jay Hineman¹, James B. Polly¹, Gary Koplik¹, Ken Ball¹, Paul Bendich^{1,4}, Joseph D'Addezio², Gregg A. Jacobs², Tamay Özgökmen³

¹Geometric Data Analytics, Inc., Durham, NC, USA

²Ocean Dynamics and Prediction, Naval Research Laboratory, Stennis Space Center, MS, USA

³Rosenstiel School of Marine and Atmospheric Science, University of Miami, FL, USA

⁴Department of Mathematics, Duke University, Durham, NC, USA

Key Points:

- Current procedures for studying submesoscale oceanographic features assume independence between features identified at different times.
- Statistics from these methods oversample features and cannot determine the lifetime evolution of the transient submesoscale processes.
- We apply the Topological Feature Tracking algorithm to identify and track eddies over time, which yields unique, time-varying statistics.

Abstract

Current state-of-the art procedures for studying modeled submesoscale oceanographic features have made a strong assumption of independence between features identified at different times. Therefore, all submesoscale eddies identified in a time series were studied in aggregate. Statistics from these methods are illuminating but oversample identified features and cannot determine the lifetime evolution of the transient submesoscale processes. To this end, the authors apply the Topological Feature Tracking (TFT) algorithm to the problem of identifying and tracking submesoscale eddies over time. TFT allows a user to identify submesoscale eddies as critical points on a set of time-ordered scalar fields and associate the points between consecutive timesteps. The procedure yields tracklets which represent spatio-temporal displacement of eddies. Thus the time-dependent behavior of submesoscale eddies can be studied. We analyze the submesoscale eddy dataset produced by TFT, which yields unique, time-varying statistics on this currently under-explored phenomenon.

Plain Language Summary

Current state-of-the art procedures for studying small-scale features in the ocean do not take the effects of time into account. Instead, features like small vortices are studied as a single population across many points in time. This method has provided oceanographers with many valuable insights. New insights can be added by identifying vortices and then tracking them over time to study their behavior through an algorithm designed to identify and track features on a grid.

1 Introduction

Submesoscale eddies are important ocean features which occupy length scales between large-scale forcings and micro-scale dissipation. Their larger, mesoscale counterparts are well studied, yet submesoscale currents have, until recently, received less attention despite the important role played in a variety of oceanic transport phenomena. In addition to influencing the transport of nutrients (Lévy et al., 2018) and pollutants (Poje et al., 2014), submesoscale currents form an important link in the turbulent energy cascade and the global oceanic circulation (see McWilliams, 2016, for a summary of submesoscale eddy dynamical theory, observational findings, and modeling approaches).

Studies considering the temporal evolution of mesoscale eddies have been performed (e.g., Chelton et al., 2007; Kurian et al., 2011; Faghmous et al., 2015), but similar investigations have yet to be done for the submesoscale. Statistical summaries of submesoscale eddy properties, behavior, and lifetime evolution are of interest to multiple communities as the nature of these disturbances inform both modeling approaches to simulate eddy dynamics, and satellite altimetry data assimilation.

While dissipation-scale phenomena are typically unresolved and parameterized with subgrid-scale closure models, the “intermediate” length scales occupied by submesoscale eddies are being resolved in models such as the Navy Coastal Ocean Model (NCOM; Barron et al., 2006) and the Regional Oceanic Modeling System (ROMS; Shchepetkin & McWilliams, 2005). Time tracking and statistical reporting of submesoscale eddies in these models is not currently done but would provide additional insight on eddy lifetime, directionality, and behavior. This information is useful for model evaluation, e.g., inspecting performance of eddy viscosity and parameterized closure schemes. Furthermore, statistical summaries of transient submesoscale eddy behavior is needed for data assimilation efforts (D’Addezio et al., 2019) and has motivated the statistical investigations in D’Addezio et al. (2020).

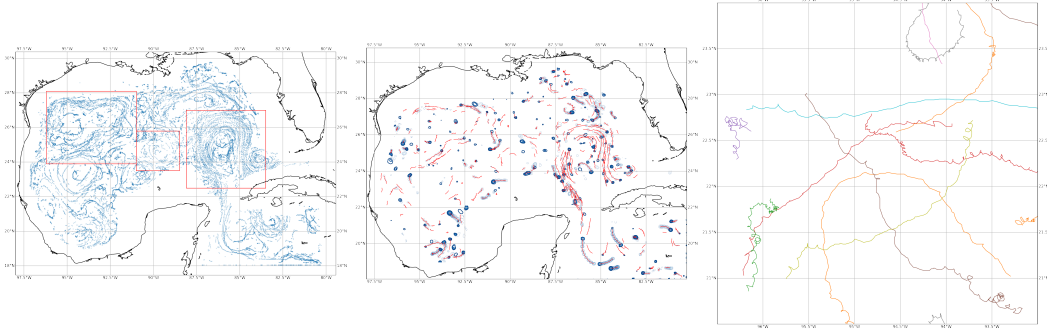


Figure 1: Left to right: (1) Submesoscale eddies identified in space and time depicted as blue points in the Gulf of Mexico. Zones 1, 2 and 3 (west to east) enclose mesoscale features which transport eddies. Eddy characteristics in these zones are explored in the following sections. (2) Submesoscale eddies being tracked through time via TFT. Solid line contours are eddies identified at January 5, 2016 03:00. Dotted line contours depict eddy locations over the previous five days. This subset depicts only tracks of 25km or longer. (3) Selection of tracks of eddies lasting for 15 days or more. These relatively long lived tracks demonstrate both the cyclic behavior and transport behavior of the eddies.

62 In this study we apply the algorithm (henceforth referred to as Topological Fea-
 63 ture Tracking, or TFT) introduced in Soler et al. (2018) to the problem of submesoscale
 64 eddy identification and temporal association. In this way, we extend the study of D’Addezio
 65 et al. (2020) by computing statistics of eddy lifetimes and trajectories to supplement the
 66 time-independent statistical analysis presented therein. Using one year of NCOM simu-
 67 lation data, we provide statistical summaries of eddy speed, lifespan, and displacement
 68 in aggregate over the Gulf of Mexico. We also provide analysis of these characteristics
 69 conditioned on season and regions selected for the presence of mesoscale features. While
 70 extending the technique used in D’Addezio et al. (2020) with the TFT-based method,
 71 we are introducing the community to the TFT approach in the context of surface-based
 72 submesoscale eddies.

73 2 Method

74 In this section we give a brief description of the TFT algorithm (Section 2.2), along
 75 with the elementary topological data analysis (TDA) concepts needed to understand it
 76 (Section 2.1). For more details on TFT and TDA in general, see Soler et al. (2018) and
 77 Edelsbrunner and Harer (2010), respectively. Finally, we describe the Okubo–Weiss pa-
 78 rameter used to generate the scalar field to which we apply TFT (Section 2.3).

79 2.1 Persistence Diagrams

80 Suppose that f is a *scalar field*, that is, a real-valued function on some domain U .
 81 The domain can be of arbitrary dimension and shape and we do not need to make any
 82 assumptions about the smoothness of f . For a working example, suppose U is any of the
 83 two-dimensional squares shown on the left side of Figure 2, with the values of f indicated
 84 by the color bar. The *persistence diagrams* of f provide a compact summary of the lo-
 85 cation and importance of topological features as observed by f . More precisely, consider
 86 $U_\alpha = \{x \in U \mid f(x) \leq \alpha\}$. As the threshold value α increases, these create a nested
 87 *filtration of sublevel sets* that start with the empty set and finish with U itself. Along
 88 the way, topological features such as *connected components* and *holes* are created and

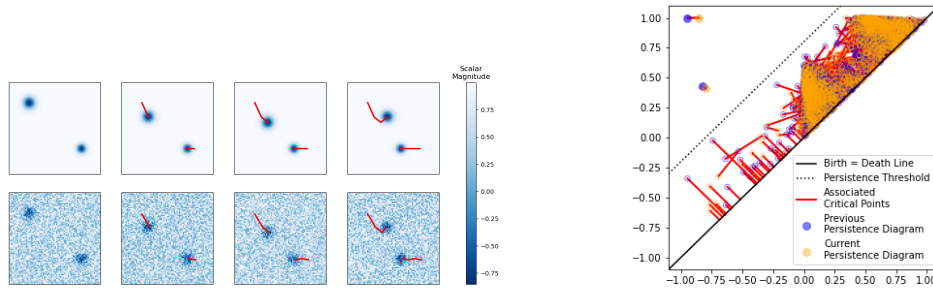


Figure 2: Illustration of TFT algorithm on a notional example: Left: Tracking two Gaussian features on a time-ordered series of scalar fields. Right: Matching between persistence diagrams (blue dots and orange dots) associated to scalar fields at $t = 2, 3$, respectively.

89 then subsequently destroyed, each of which corresponds (Milnor, 1963) to a *critical point*
 90 of f that occurs at a *critical value*. The birth and death critical values of each feature
 91 are plotted as dots in the plane, and the multi-set of such dots, along with the major di-
 92 agonal $y = x$, forms the persistence diagram $D(f)$ of the scalar field. Two such di-
 93 agrams can be seen on the right side of Figure 2, where blue (orange) dots correspond to
 94 features in the scalar fields in the second (third) columns, bottom row. The *persistence*
 95 of a dot is the difference between its death and birth values (i.e, the vertical distance to
 96 the major diagonal). Higher-persistence dots tend to be less likely to be noise. For ex-
 97 ample, all of the example scalar fields have two prominent connected components indi-
 98 cated by the two dots far from the major diagonal.

99 Persistence diagrams have two important properties that we exploit in this paper.
 100 First, they are *stable to noise* in a precise sense. The *Wasserstein distance* between two
 101 diagrams can be defined as the cost of an optimal matching between the dots in the di-
 102 agrams, where dots can be matched to the major diagonal if needed; the right side of
 103 Figure 2 shows an optimal matching. Precise theorems (Cohen-Steiner et al., 2007) bound
 104 the Wasserstein distance between two diagrams $D(f), D(g)$ in terms of the ℓ_∞ distance
 105 between the scalar fields f, g . In particular, this guarantees that the diagrams associated
 106 to a smoothly time-varying sequence of scalar fields will themselves form a time-varying
 107 sequence, which facilitates the TFT algorithm. Second, various theorems (Edelsbrunner
 108 et al., 2006; Laudenbach, 2013) guarantee the following: given a two-dimensional scalar
 109 field f and a threshold value ϵ , there exists a simplified scalar field g with exactly the
 110 same critical point structure of f except that all critical points of persistence less than
 111 ϵ have been removed. For example, with ϵ being the distance between the major di-
 112 agonal and the dotted line on the right side of Figure 2, the scalar fields in the top row on
 113 the left are the topological simplifications of the scalar fields in the bottom row.

114 2.2 Topological Feature Tracking

115 Now suppose that we have a time-ordered sequence f_1, \dots, f_T of scalar fields, such
 116 as the four fields across either row on the left of Figure 2, all defined on the same do-
 117 main U . Computing persistence leads to a time-ordered sequence $D(f_1), \dots, D(f_T)$ of
 118 persistence diagrams. The user has the option of choosing a persistence threshold to topo-
 119 logically simplify the scalar fields as desired. Then the TFT algorithm connects certain
 120 critical points to produce a series of *tracks*, as follows.

121 Consider a time-adjacent pair of (possibly simplified) scalar fields f_i and f_{i+1} . Each
 122 dot in the two diagrams corresponds to a topological feature, and has associated to it
 123 a pair of critical points in U , one which created the feature and one which destroyed it.
 124 The *lifted Wasserstein* distance of Soler et al. (2018) defines the cost of associating two
 125 dots in $D(f_i)$ and $D(f_{i+1})$ as a (user-specified) weighted combination of the distance be-
 126 tween the pair of dots in the persistence diagram and the geometric distance between
 127 the associated critical points in the domain U , and an optimal matching between the two
 128 diagrams is then computed via this cost function. If this optimal matching connects two
 129 dots, then a track segment is drawn between their associated critical points. If it con-
 130 nects a dot at time i with the diagonal at time $t + 1$, then a track segment ends. If it
 131 connects a dot at time $i+1$ with the diagonal at time i , a new track segment is started.
 132 The end result, over all time steps in the sequence, is a set of tracks which move in time
 133 through the domain U .

134 Figure 2 shows the outputted tracks for our notional example, indicated as thick
 135 red lines on the left side of the figure. Figure 1 shows tracks for submesoscale eddies, iden-
 136 tified by the same procedure and further described in the following sections.

137 The matching procedure described above must be applied to each consecutive pair
 138 of persistence diagrams in the time series. Computationally, this may be done in par-
 139 allel so long as the time order is maintained. Once matching is completed for all con-
 140 secutive time steps, the matchings of associated critical pairs may be applied to coordi-
 141 nates in the domain to combine the track segments and form full tracks of the iden-
 142 tified features.

143 2.3 Okubo–Weiss Parameter

144 The above describes the TFT method applied to a time-ordered series of arbitrary
 145 scalar fields. Our application is concerned with a specific scalar field, called the *Okubo–*
 146 *Weiss* parameter.

147 Following D’Addezio et al. (2020), this is defined as

$$148 \quad W = S_n^2 + S_s^2 - \zeta^2 \quad (1)$$

149 S_n and S_s are the normal and shear components of the strain respectively while ζ rep-
 150 represents relative vorticity. A location at which $|\zeta| > S_n^2 + S_s^2$ implies $W < 0$ thus a
 151 high relative vorticity at that location. Regions having this quality may be interpreted
 as eddies.

152 3 Data & Procedure

153 The dataset used in this paper is a year-long simulation of the Gulf of Mexico gener-
 154 ated by the Navy Coastal Ocean Model (NCOM). The dataset has a spatial resolu-
 155 tion of one kilometer. The data were provided with temporal resolution of three hours.
 156 The time period of this dataset ranges from January 1, 2016 at 00:00 to December 31,
 157 2016 at 21:00. Two derivative datasets were generated from the NCOM simulation. The
 158 first is an exact replication of the dataset generated in D’Addezio et al. (2020). We call
 159 this the “masked” dataset—where all Okubo–Weiss values outside of the submesoscale
 160 eddy region are masked, and only eddies remain (see D’Addezio et al., 2020 for details).
 161 The second dataset is a less stringent version of the first in which the same procedure
 162 is followed until the normalized Okubo–Weiss field W_N is generated. We refrain from
 163 applying the second smoothing filter and circularity test from this dataset; we therefore
 164 refer to it as “unmasked” as the entire Okubo–Weiss field remains, thus tasking the TFT
 165 algorithm to perform eddy identification.

166 We apply the TFT algorithm to the negative portions of each scalar field in both
 167 datasets. The negative portions of the scalar fields represent vortices. We found that lim-
 168 iting the field to only negative values resulted in the best track quality.

169 The output of the TFT algorithm is a set of tracks representing the historical be-
 170 havior of individual submesoscale eddies in the Gulf of Mexico. Two mild postprocess-
 171 ing routines were applied to this set of tracks. We first removed tracks which began or
 172 ended on the boundary of the Gulf of Mexico. These erroneous tracks are caused by the
 173 abrupt end of the scalar field at its edges. We also applied a filter which removed any
 174 tracks whose average speed was greater than the maximum surface speed at any point
 175 in the NCOM simulation. A subset of the resulting tracks can be seen in the middle and
 176 right images of Figure 1.

177 4 Results

178 In this section we provide insights gleaned from tracking submesoscale eddies iden-
 179 tified in the Okubo–Weiss field. In Section 4.1 we share figures which depict large scale
 180 features’ influence on submesoscale eddy transport. In Section 4.2 we provide descrip-
 181 tive statistics of submesoscale eddy behavior observed through tracks identified using TFT.

182 4.1 Identifying Seasonal Mesoscale Patterns via Submesoscale Tracks

183 Mesoscale features are responsible for transporting submesoscale eddies through-
 184 out the Gulf of Mexico. By tracking those submesoscale eddies as they are transported,
 185 we are able to gain insight into the evolving behavior of the mesoscale phenomena as well.
 186 Figure 3 depicts this behavior in large scale features through their influence on subme-
 187 soscale eddies. Each frame of Figure 3 represents three months of tracks of submesoscale
 188 eddies ≥ 25 km in length. Beginning in the top left image (winter), the greatest sub-
 189 mesoscale eddy track density appears in the Loop Current passing north between Cuba
 190 and the Yucatán Peninsula and exiting the Gulf between the tip of Florida and north-
 191 ern coast of Cuba. We are able to watch the continued deformation of this Loop Cur-
 192 rent throughout the year by observing its shifting impact on the trajectories of local sub-
 193 mesoscale eddies. By the spring (bottom left image) the Loop Current has split into a
 194 lower current exiting the gulf to the east and a mesoscale eddy off the western coast of
 195 Florida. By the summer (top right) this large eddy has moved west, and a greater den-
 196 sity of tracks appear in the east bound current. Finally in the fall the large mesoscale
 197 eddy appears to have largely dissipated while the current continues to carry a high den-
 198 sity of eddies to the east. Across all seasons, the submesoscale tracks do not follow any
 199 consistent directional pattern. Their flow appears predominantly determined by the large-
 200 scale background flow, that being dictated primarily by both the synoptic jet and the
 201 interior mesoscale eddies. This is in contrast with the mesoscale eddy field which is known
 202 to propagate westward outside the influence of boundary currents (Chelton et al., 2007).

203 4.2 Statistical Summary of Tracks

204 We provide descriptive statistics of tracks generated by features identified on the
 205 Okubo–Weiss fields in Table 1. We calculate track statistics in aggregate within the Gulf
 206 of Mexico for an entire year as well as on subsets of the tracks. We subset tracks tem-
 207 porally by season (winter, spring, summer and fall) as well as spatially in three “zones”
 208 associated with large scale features. These zones are depicted in the left image of Fig-
 209 ure 1. These zones are labeled Zone 1, Zone 2 and Zone 3 from west to east. Zone 1 is
 210 an irregularly shaped, counterclockwise flow. Zone 2 is a circular, counterclockwise pat-
 211 tern. Zone 3 is a clockwise flow passing north between Cuba and the Yucatán Peninsula,
 212 reaching its zenith and turning south before passing between the Florida Keys and Cuba’s
 213 northern coast.

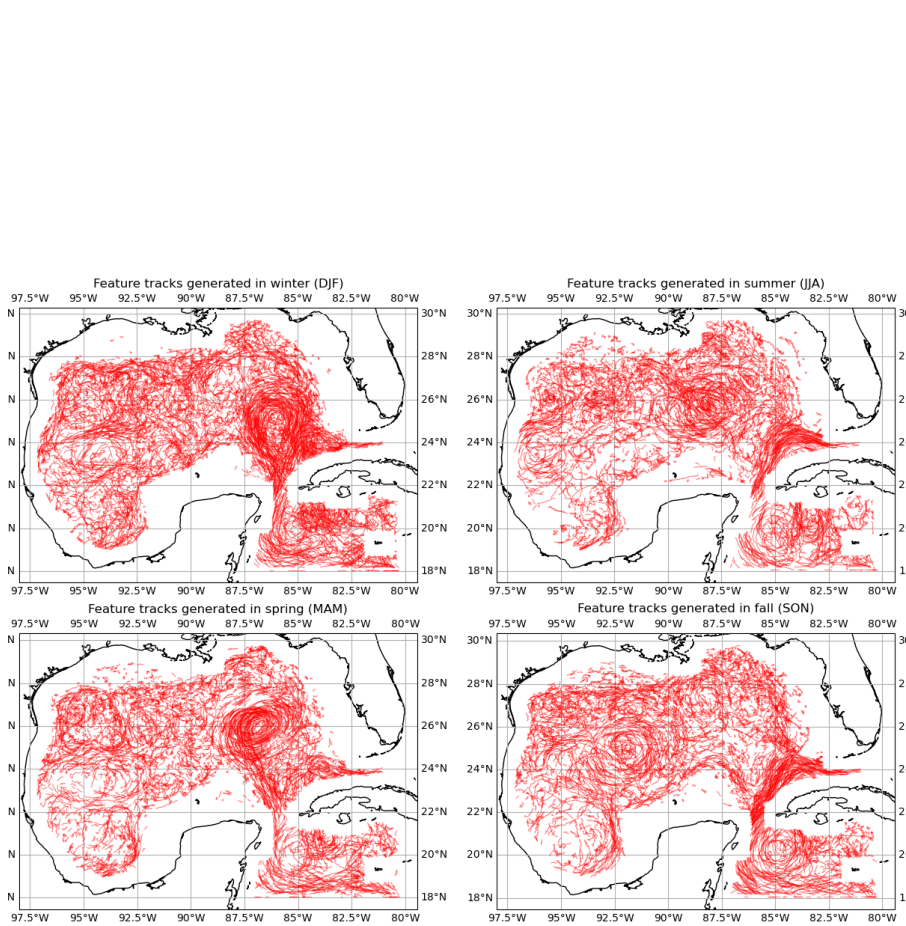


Figure 3: Illustration of submesoscale eddy behavior in aggregate over four seasons of the NCOM dataset. We can see changes in the large scale features responsible for transporting submesoscale eddies here. Tracks have been filtered down to those greater than or equal to 25km for these images.

214 Broadly, eddies in the Gulf of Mexico tend to move fastest in the spring and sum-
 215 mer. However, the seasonal variance is low. Overall, submesoscale eddy velocity is $O(0.5$
 216 $m/s)$, furthering previous results which showed mesoscale and submesoscale horizontal
 217 velocities to be similar (Capet et al., 2008). If, as we have documented, the submesoscale
 218 eddy motion is largely a function of the jet and mesoscale eddies (Figure 1), this hor-
 219 izontal velocity proportionality is consistent

220 Lifespans tend to be longer in the winter and fall. This is likely due to the known
 221 relationship between submesoscale generation and maintenance, and the depth of the mixed
 222 layer (McWilliams, 2016). Using this relationship, one can calculate a mixed-layer de-
 223 formation radius that dictates the maximum size of submesoscale eddies as a function
 224 of mixed-layer depth. In the summer, the mixed layer shoals in the presence of strong
 225 surface heating, dramatically reducing the mixed-layer deformation radius. With a 1-
 226 km horizontal resolution, this NCOM simulation cannot support the generation and main-
 227 tenance of such small features, leading to a decline in the number of identified subme-
 228 soscale eddies during this season (D’Addezio et al., 2020). As is found here, any subme-
 229 soscale eddy generated by the model during this time period is likely to be short lived
 230 because mixed layer dynamics are not favorable. This is further supported by the sea-
 231 sonality of the submesoscale eddy sample size (Table 1; last column). In contrast, win-
 232 ter features much deeper mixed layers, and can therefore support the creation of more,
 233 relatively larger submesoscale eddies and allow them to propagate longer in the more fa-
 234 vorable mixed layer environment.

235 Finally, displacements tend to be similar across seasons for the unmasked group
 236 while eddies identified in the masked dataset tend to travel further during the winter and
 237 fall months. Note that both distances and lifetimes are greater for the unmasked fields,
 238 compared with the masked fields. This is due to the limiting nature of traditional eddy
 239 identification methods (e.g., D’Addezio et al., 2020). Certain criteria for identification,
 240 e.g., “circularity” may change over the eddy lifetime such that the feature fails to meet
 241 the identification criteria at some instances. This is an advantage of using TFT for this
 242 purpose so as to capture a more complete lifespan of an eddy rather than omit features
 243 in the middle of their evolution due to lacking circularity or other identification crite-
 244 ria.

	Speed (m/s)		Lifespan (h)		Displacement (km)		Sample Size	
	Unmasked	Masked	Unmasked	Masked	Unmasked	Masked	Unmasked	Masked
	Mean (St. Dev.)	Mean (St. Dev.)	Mean (St. Dev.)	Mean (St. Dev.)	Mean (St. Dev.)	Mean (St. Dev.)		
GoM Aggregate	0.4436 (0.2343)	0.3808 (0.2124)	17.8 (28.8)	12.3 (26.0)	30.9 (60.4)	16.2 (31.4)	655,727	119,775
GoM Winter (DJF)	0.4184 (0.2333)	0.3760 (0.2171)	19.0 (30.5)	13.5 (27.6)	31.3 (62.0)	17.4 (33.7)	182,522	31,319
GoM Spring (MAM)	0.4726 (0.2367)	0.3949 (0.2167)	16.7 (25.7)	11.1 (20.7)	31.4 (58.5)	15.4 (27.3)	171,134	31,292
GoM Summer (JJA)	0.4703 (0.2354)	0.3928 (0.2156)	15.8 (25.1)	11.6 (27.6)	29.1 (54.9)	15.8 (32.8)	154,453	28,545
GoM Fall (SON)	0.4133 (0.2241)	0.3586 (0.1966)	19.4 (33.3)	13.0 (27.5)	31.6 (66.0)	16.1 (31.7)	147,618	28,619
Zone 1 Aggregate	0.4316 (0.2154)	0.3457 (0.1689)	18.4 (30.0)	12.8 (26.4)	30.9 (58.9)	15.2 (28.6)	141,626	27,081
Zone 1 Winter	0.3862 (0.2034)	0.3205 (0.1598)	20.6 (33.7)	14.6 (29.3)	31.1 (61.2)	16.1 (30.1)	38,219	6,859
Zone 1 Spring	0.4556 (0.2189)	0.3526 (0.1697)	17.8 (26.8)	11.3 (20.2)	32.0 (58.2)	13.8 (22.9)	39,754	7,848
Zone 1 Summer	0.4622 (0.2187)	0.3596 (0.171)	16.3 (25.7)	11.6 (26.5)	29.5 (53.7)	14.4 (29.1)	35,998	6,737
Zone 1 Fall	0.4200 (0.2106)	0.3501 (0.1727)	19.1 (33.4)	14.2 (29.8)	30.8 (63.0)	17.2 (32.8)	27,655	5,637
Zone 2 Aggregate	0.4315 (0.2172)	0.3725 (0.1887)	16.8 (29.0)	12.8 (27.1)	26.6 (47.8)	16 (30.9)	24,571	5,773
Zone 2 Winter	0.4137 (0.2101)	0.3528 (0.1745)	18.2 (29.8)	13.8 (26.7)	27.5 (47.4)	16.1 (27.3)	6,601	1,506
Zone 2 Spring	0.4304 (0.2187)	0.3523 (0.1837)	15.6 (25.9)	12.2 (20.9)	25.2 (44.6)	14.4 (22.4)	5,576	1,443
Zone 2 Summer	0.4887 (0.2317)	0.4427 (0.2218)	13.6 (21.6)	11.3 (28.8)	25.2 (46.5)	17.0 (35.2)	5,481	1,245
Zone 2 Fall	0.4040 (0.2019)	0.3542 (0.1631)	18.8 (34.9)	13.6 (30.7)	27.8 (51.6)	16.6 (36.5)	6,913	1,579
Zone 3 Aggregate	0.5167 (0.2513)	0.4917 (0.2566)	14.8 (24.3)	12.0 (22.3)	29.3 (52.9)	21.0 (38.0)	93,578	19,608
Zone 3 Winter	0.5196 (0.2581)	0.5177 (0.2642)	16.4 (25.6)	12.5 (23.6)	33.1 (59.6)	23.1 (42.2)	29,903	5,849
Zone 3 Spring	0.5621 (0.2464)	0.5459 (0.2562)	13.8 (21.2)	10.9 (17.2)	30.5 (54.0)	21.9 (37.6)	23,629	4,813
Zone 3 Summer	0.5275 (0.2458)	0.4833 (0.2536)	13.5 (21.5)	11.3 (22.2)	27.1 (47.8)	19.3 (35.5)	22,881	4,773
Zone 3 Fall	0.4348 (0.2333)	0.4023 (0.2238)	15.3 (28.8)	13.2 (25.4)	23.7 (43.8)	18.8 (34.5)	17,165	4,173

Table 1: A selection of descriptive statistics of submesoscale eddy tracks across the Gulf of Mexico and in each of the three zones depicted in Figure 1. Statistics for the Gulf of Mexico and each zone are calculated in aggregate as well as by season.

245 5 Conclusions

246 Our application of TFT to submesoscale eddy tracking provides new insights into
 247 the behavior of small scale structures in the ocean. Through studying the movement pat-
 248 terns of submesoscale eddies, we improve our understanding of the mesoscale phenom-
 249 ena that are responsible for their transport. Neither labeled training data nor long train-
 250 ing epochs were required for tracking eddies in the Gulf of Mexico. TFT may be sim-
 251 ilarly applied to any section of the ocean and indeed to any evolving scalar field.

252 Future work may focus on tracking meso- and submesoscale eddies entangled within
 253 the same field. Further modifying the Lifted Wasserstein distance function to penalize
 254 incorrect matchings in a nonlinear manner will improve the method broadly. Addition-
 255 ally, an automated method of suggesting or selecting weight parameters and the persis-
 256 tence threshold may be explored.

257 Open Research

258 Data Availability Statement: Ocean surface velocity data, used to identify and track
 259 features in this study, were obtained via the Navy Coastal Ocean Model (NCOM). The
 260 solution data used herein was generated using the same NCOM modeling framework (i.e.,
 261 domain, boundary and initial conditions, numerical and physical parameterizations, etc.)
 262 as described in D’Addezio et al. (2020) (<https://doi.org/10.1175/JPO-D-19-0100.1>).

263 Acknowledgments

264 Research by the first six authors was partially supported by the DARPA Ocean of Things
 265 project, under contract N6600121C4006. Joseph M. D’Addezio was funded by the Of-
 266 fice of Naval Research (ONR) under grant N0001421WX02086. Gregg Jacobs and Tamay
 267 Özgökmen were funded by the DARPA Ocean of Things project under contract HR0011150953.
 268 This document has been cleared for public release under Distribution Statement "A" (Ap-
 269 proved for Public Release, Distribution Unlimited). The views, opinions and/or findings
 270 expressed are those of the authors and should not be interpreted as representing the of-
 271 ficial views or policies of the Department of Defense or the U.S. Government.

272 References

- 273 Barron, C. N., Kara, A. B., Martin, P. J., Rhodes, R. C., & Smedstad, L. F. (2006).
 274 Formulation, implementation and examination of vertical coordinate choices
 275 in the global navy coastal ocean model (ncom). *Ocean Modelling*, *11*(3-4),
 276 347–375.
- 277 Capet, X., McWilliams, J., Molemaker, M., & Shchepetkin, A. (2008). Mesoscale to
 278 submesoscale transition in the california current system part i: Flow structure,
 279 eddy flux, and observational tests. *J. Phys. Oceanogr.*, *38*, 29-43.
- 280 Chelton, D. B., Schlax, M. G., Samelson, R. M., & de Szoeke, R. A. (2007). Global
 281 observations of large oceanic eddies. *Geophysical Research Letters*, *34*(15).
- 282 Cohen-Steiner, D., Edelsbrunner, H., & Harer, J. (2007, January). Stability of per-
 283 sistence diagrams. *Discrete Comput. Geom.*, *37*(1), 103–120. Retrieved from
 284 <http://dx.doi.org/10.1007/s00454-006-1276-5> doi: 10.1007/s00454-006-
 285 -1276-5
- 286 D’Addezio, J. M., Jacobs, G. A., Yaremchuk, M., & Souopgui, I. (2020). Sub-
 287 mesoscale eddy vertical covariances and dynamical constraints from high-
 288 resolution numerical simulations. *Journal of Physical Oceanography*, *50*(4),
 289 1087–1115.
- 290 D’Addezio, J. M., Smith, S., Jacobs, G. A., Helber, R. W., Rowley, C., Souopgui,
 291 I., & Carrier, M. J. (2019). Quantifying wavelengths constrained by simu-
 292 lated swot observations in a submesoscale resolving ocean analysis/forecasting

- 293 system. *Ocean Modelling*, 135, 40–55.
- 294 Edelsbrunner, H., & Harer, J. (2010). *Computational topology: an introduction*.
 295 AMS.
- 296 Edelsbrunner, H., Morozov, D., & Pascucci, V. (2006). Persistence-sensitive sim-
 297 plification functions on 2-manifolds. In *Proceedings of the twenty-second annual*
 298 *symposium on computational geometry* (pp. 127–134).
- 299 Faghmous, J. H., Frenger, I., Yao, Y., Warmka, R., Lindell, A., & Kumar, V. (2015).
 300 A daily global mesoscale ocean eddy dataset from satellite altimetry. *Scientific*
 301 *data*, 2(1), 1–16.
- 302 Kurian, J., Colas, F., Capet, X., McWilliams, J. C., & Chelton, D. B. (2011). Eddy
 303 properties in the california current system. *Journal of Geophysical Research:*
 304 *Oceans*, 116(C8).
- 305 Laudenbach, F. (2013). A proof of morse’s theorem about the cancellation of critical
 306 points. *Comptes Rendus de l’Academie des Sciences*, 483–488.
- 307 Lévy, M., Franks, P. J. S., & Smith, K. S. (2018). The role of submesoscale currents
 308 in structuring marine ecosystems. *Nature communications*, 9(1), 1–16.
- 309 McWilliams, J. C. (2016). Submesoscale currents in the ocean. *Proceedings of the*
 310 *Royal Society A: Mathematical, Physical and Engineering Sciences*, 472(2189),
 311 20160117.
- 312 Milnor, J. W. (1963). *Morse theory*. Princeton University Press.
- 313 Poje, A. C., Özgökmen, T. M., Lipphardt, B. L., Haus, B. K., Ryan, E. H., Haza,
 314 A. C., . . . others (2014). Submesoscale dispersion in the vicinity of the deep-
 315 water horizon spill. *Proceedings of the National Academy of Sciences*, 111(35),
 316 12693–12698.
- 317 Shchepetkin, A. F., & McWilliams, J. C. (2005). The regional oceanic modeling
 318 system (roms): a split-explicit, free-surface, topography-following-coordinate
 319 oceanic model. *Ocean modelling*, 9(4), 347–404.
- 320 Soler, M., Plainchault, M., Conche, B., & Tierny, J. (2018). Lifted wasser-
 321 stein matcher for fast and robust topology tracking. *2018 IEEE 8th Sym-*
 322 *posium on Large Data Analysis and Visualization (LDAV)*, 23–33. doi:
 323 10.1109/ldav.2018.8739196

Figure 1.

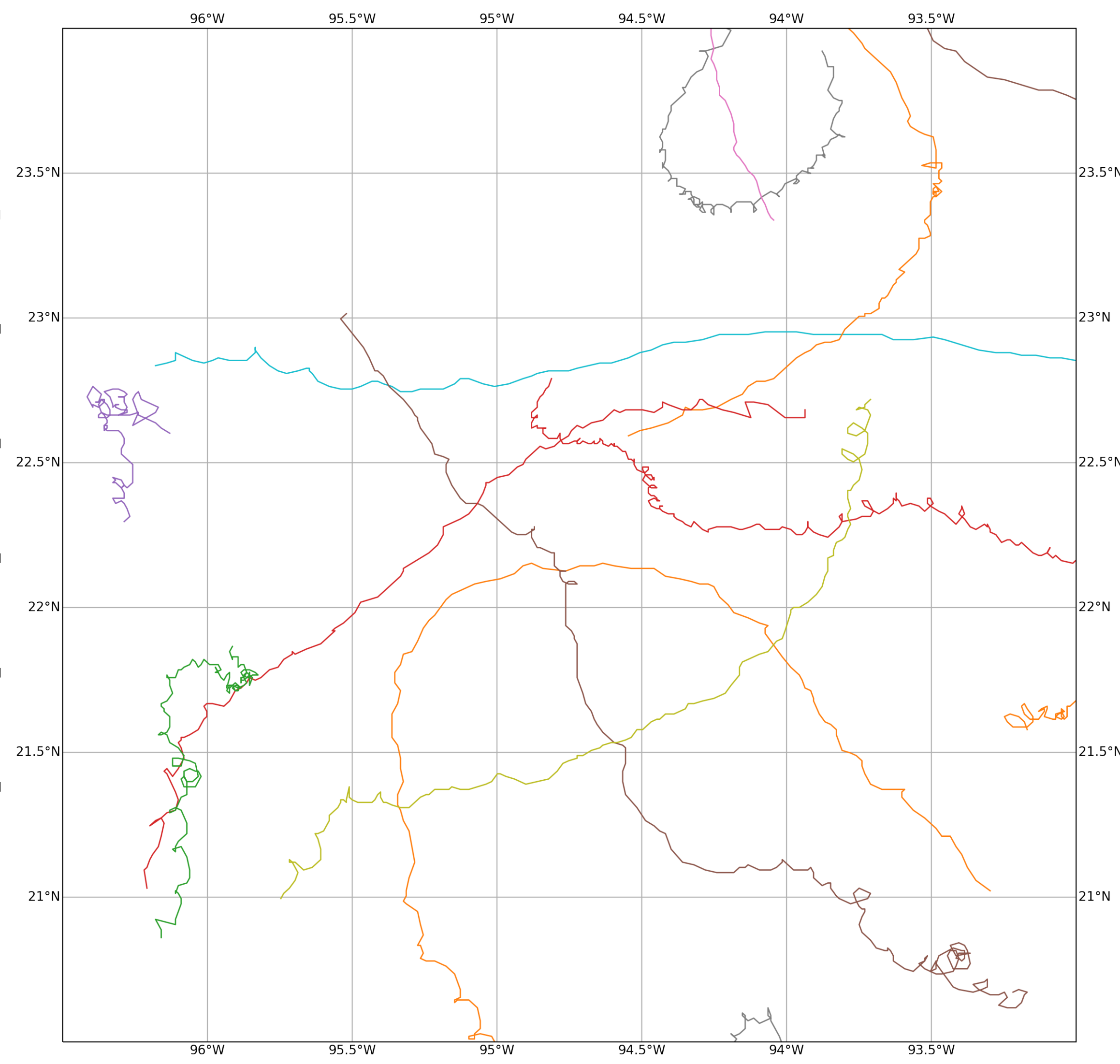
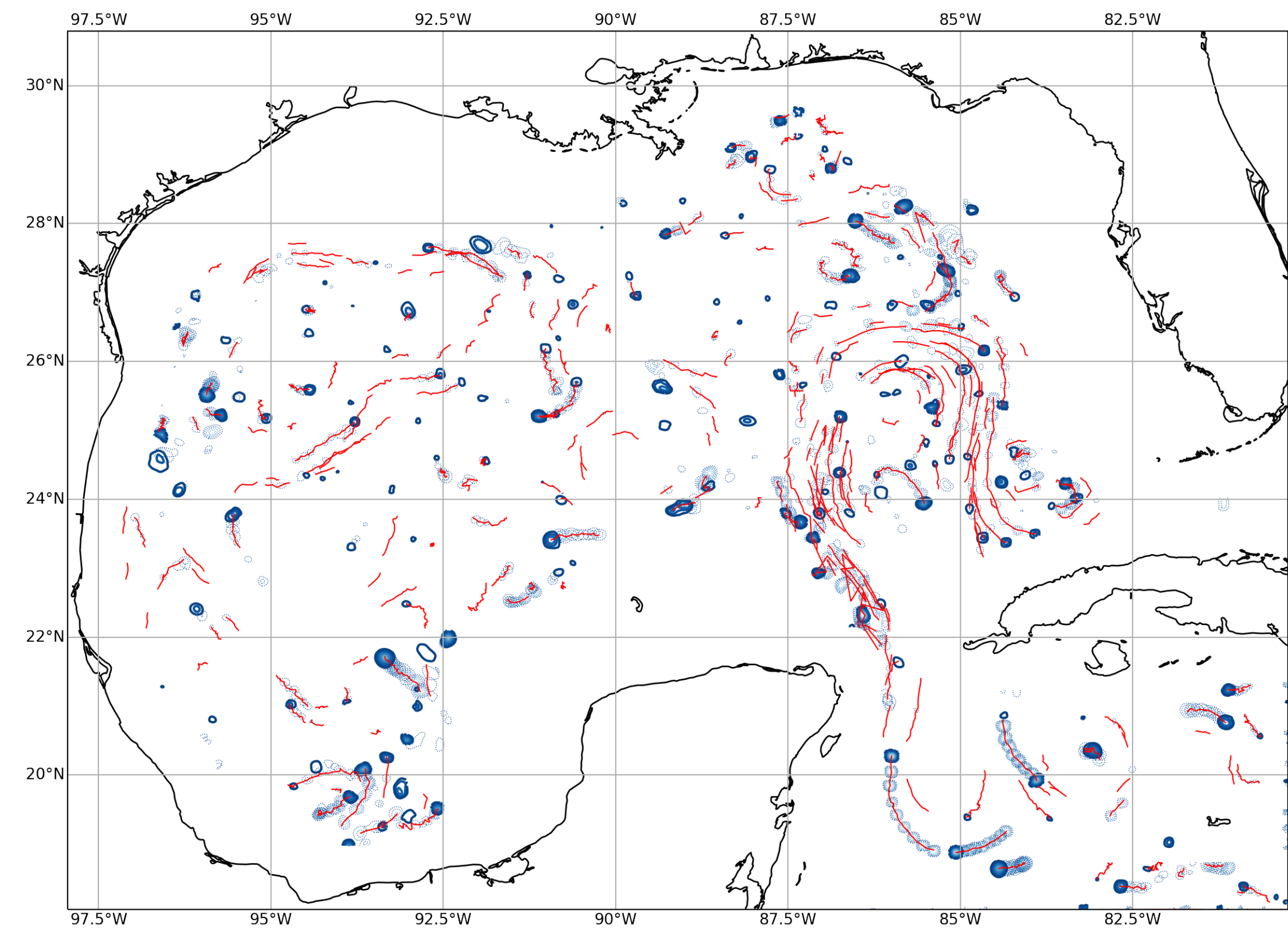
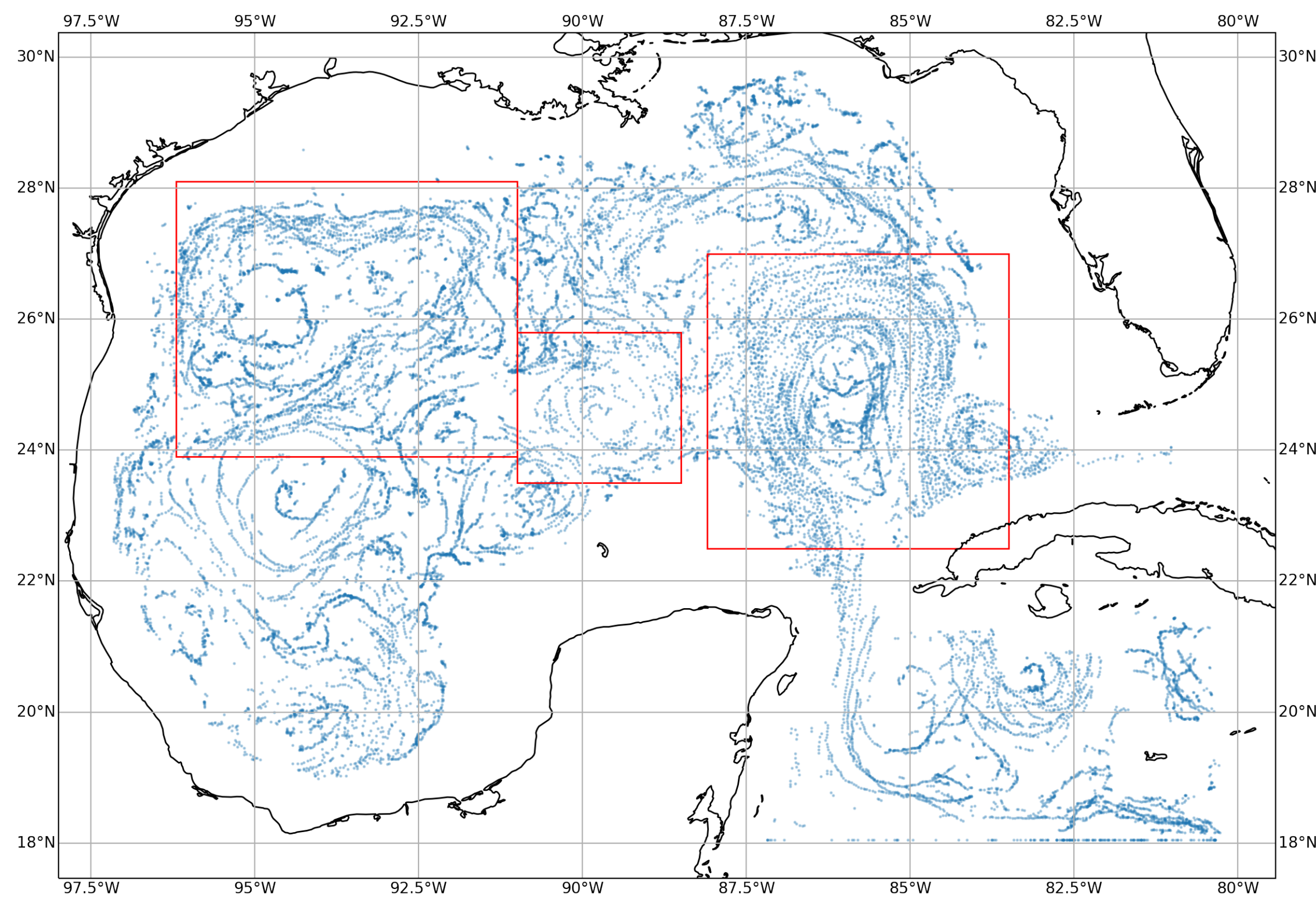


Figure 2, RHS.

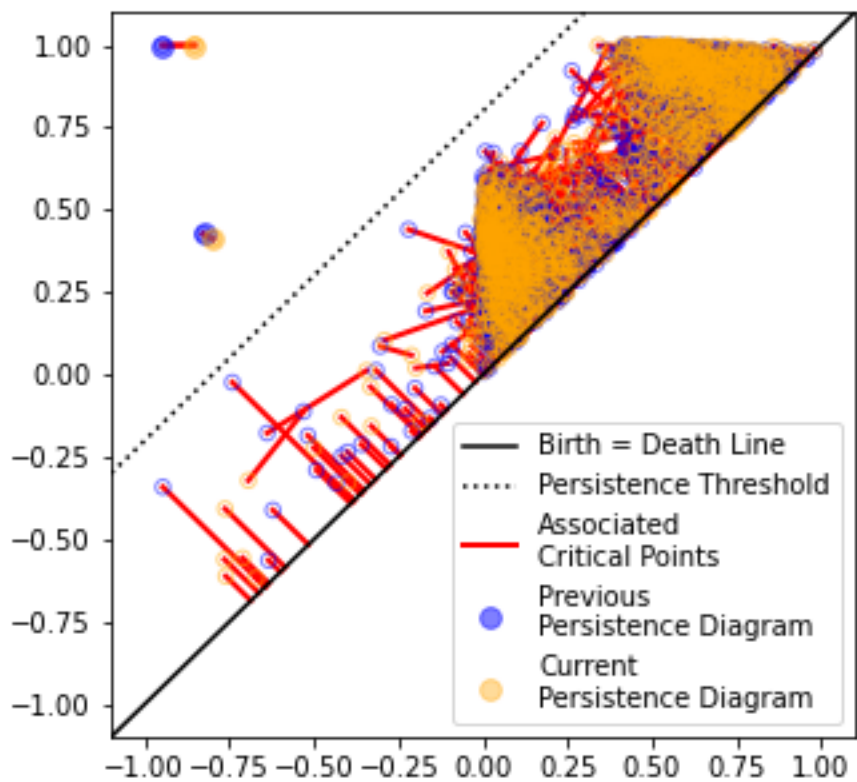
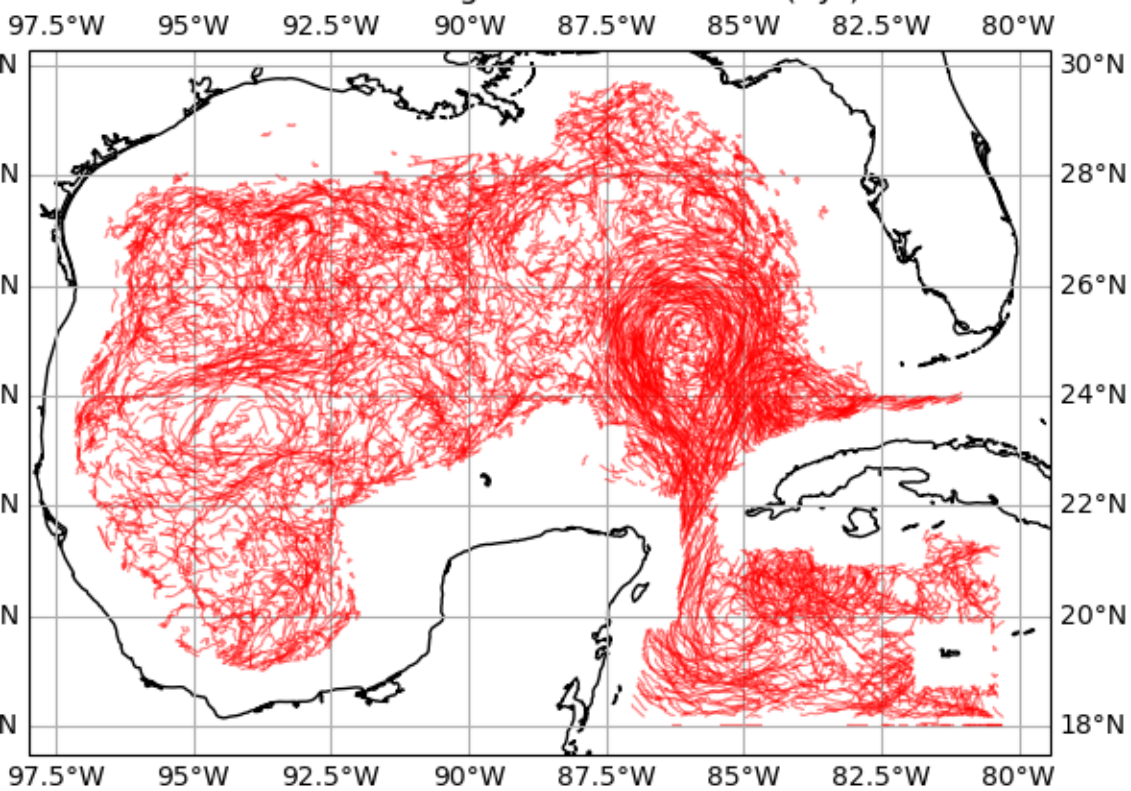
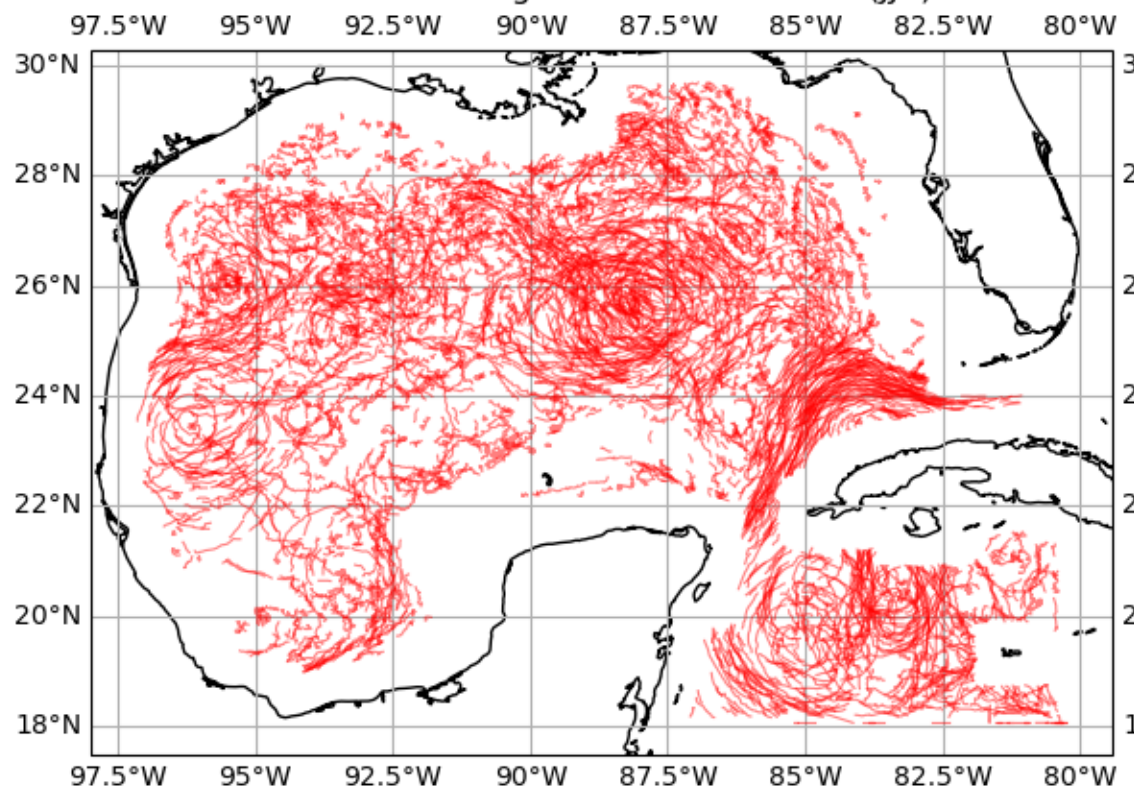


Figure 3.

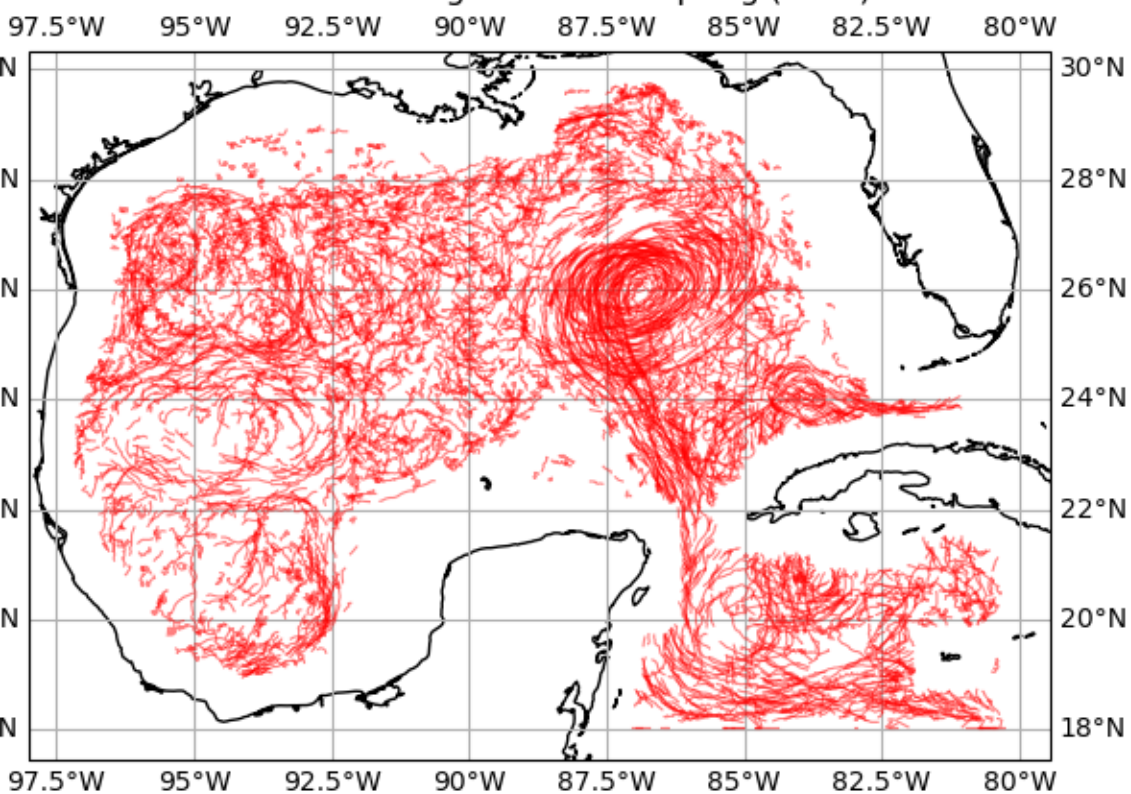
Feature tracks generated in winter (DJF)



Feature tracks generated in summer (JJA)



Feature tracks generated in spring (MAM)



Feature tracks generated in fall (SON)

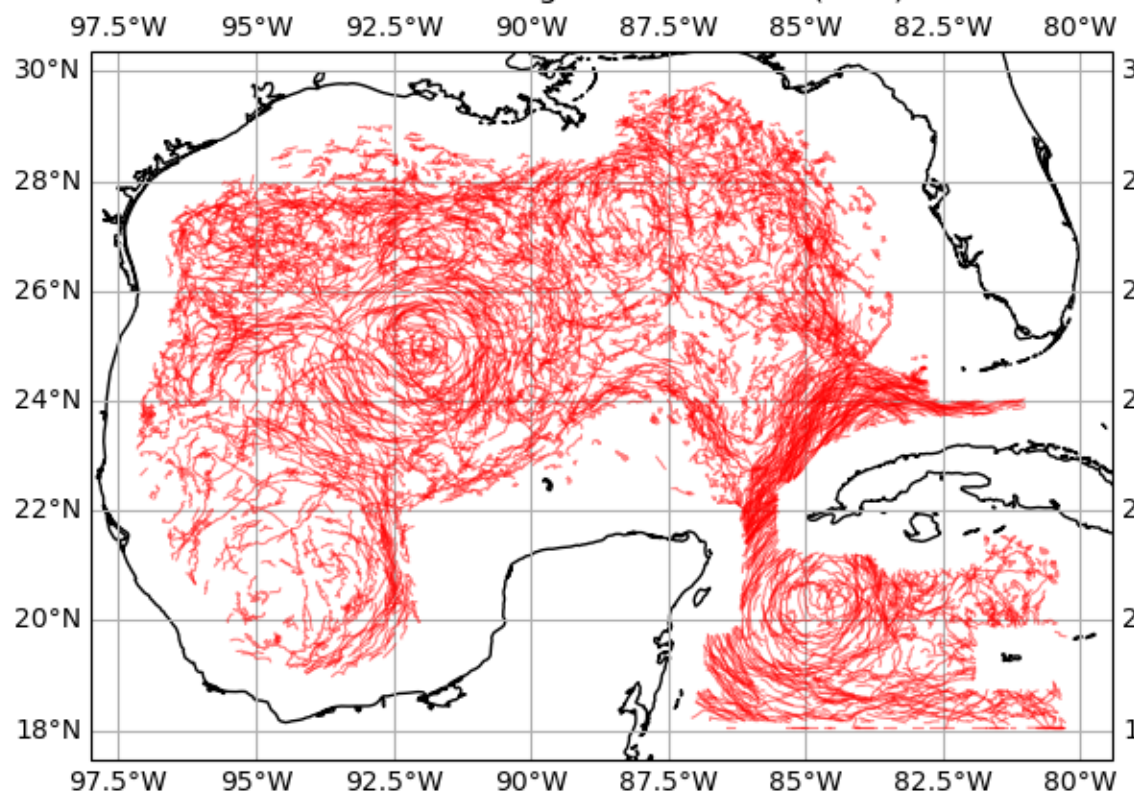


Figure 2, LHS.

